# Digital Implementation Issues on High Speed Permanent Magnet Machine FOC Drive Under Insufficient Sample Frequency

**SHIH-CHIN YANG** [1], (Senior Member, IEEE), **YU-LIANG HSU** [2], (Member, IEEE), **PO-HUAN CHOU** [3], **JYUN-YOU CHEN** [1], AND **GUAN-REN CHEN** [1], (Student Member, IEEE)

[1]Department of Mechanical Engineering, National Taiwan University, Taipei 10617, Taiwan
[2]Department of Automatic Control Engineering, Feng Chia University, Taichung 40724, Taiwan
[3]Industrial Technology Research Institute, Hsinchu 31057, Taiwan

Corresponding author: Shih-Chin Yang (scy99@ntu.edu.tw)

**ABSTRACT** This paper investigates digital implementation issues on high-speed permanent magnet (PM) machine drives. The machine operating speed is designed beyond 30krpm where the ratio of controller sample frequency over rotor $f_{sample}$ operating frequency $f_e$ is less than 5. Because microcontrollers are used in variable frequency drives to realize the field oriented control (FOC), the discretized effects must be considered to maintain the controller stability under low ratios of $f_{sample}/f_e$. In this paper, the FOC based on different digital controllers is compared specifically at low $f_{sample}/f_e$. It is shown that digital controllers using forward difference and bilinear approximation are able to maintain the drive stability if the voltage delay and inductance cross-coupling are compensated. However, the drive performance strongly depends on the accuracy of the inductance parameter. By contrast, the controller using direct digital design achieves the better FOC performance independent to machine parameters. Different types of controllers have experimentally compared to find a suited high-speed FOC drive. This paper includes the design guidance of high-speed FOC drive for PM machines with different time constants.

**INDEX TERMS** Machine drives, digital controller, discrete-time approximation, field oriented control.

## I. INTRODUCTION

High speed machine drives are widely used in applications with high power densities under size limitation, e.g. compressors, fans, drillers and spindles. Among these drives, the six-step trapezoidal control with pulse amplitude modulation [1]–[3] is typically implemented to compromise considerable acoustic noises and rotor iron losses. However from the perspective of drive efficiency, FOC with the sinusoidal current regulation is preferred [4]. Due to the limitation on sample frequency and PWM frequency, several digital implementation issues must be considered to achieve the FOC at low $f_{sample}/f_e$.

The straightforward digital implementation of FOC controller is to design in continuous-time and linearize in discrete-time. In general, the linearization can be categorized

as i) forward difference, ii) backward difference and iii) bilinear approximation (center difference) [5]–[7]. It is noted that all these three linearization methods result in the comparable performance when the microcontroller (MCU) sample frequency is $f_{sample}$ sufficient high. From the rule of thumb, the ratio of $f_{sample}/f_e$ should be larger than 10 to maintain the controller performance [8]. However considering the high speed operation with low $f_{sample}/f_e$, the degraded FOC performance and stability issue might appear [9].

For FOC drives, machine phase voltage input is manipulated by the inverter PWM. Under this effect, there is a deviation between the actual PWM voltage and the voltage command generated from the controller. This difference can be modeled by a zero order hold (ZOH) between the voltage command and actual voltage [10], [11]. The ZOH effect can be negligible when $f_{sample}/f_e$ is sufficient high. However at high speed, ZOH might result in the phase delay on the actual voltage. As reported in [10], the ZOH reflected phase

delay increases as the rotor frequency $f_e$ increases. Ideally, this phase delay is equal to $1.5f_e/f_{sample}$ when the machine is operated at steady state. In addition, ZOH also causes one step magnitude delay during the digital-to-analog voltage conversion [12], [13].

In general, FOC is implemented in the rotor-reference synchronous frame to regulate DC components of d-axis current and q-axis current $i_q$. Although high bandwidth regulation is achieved, cross-coupling between d- and q-axis inductance $L_d$, and $L_q$, must appear because the inductive voltage drop is a speed dependent function. Assuming the machine parameters $L_d$ and $L_q$ are well known, the inductance cross-coupling can be decoupled based on the complex dq current controller [14]. However, the cross-coupling decoupling performance strongly depends on the parameter accuracy. In [15], the neural network inverse and internal model control are developed for the decoupling of nonlinear cross-coupling machine drive. [16] comprehensively explains the design of internal model controller for the cross-coupling machine drive based on the pseudo-linear approximation. In addition instead of FOC, the inductance cross-coupling results in the negligible influence on the machine control if the model predictive torque control is applied [17], [18].

Considering the implementation using digital controllers, the inductance cross-coupling discretized model is developed in [9], [13], [19] for surface PM machines whereby $L_d = L_q$. By contrast for interior PM machines, dq cross-coupled difference equations [20] or flux difference equations [21] in discrete-time is developed to realize the inductance cross-coupling decoupling. However in [9], [20], [21], various nonlinear exponential functions are resultant in digital controllers due to inductive components in PM machines. Considering FOC using low-cost MCU, the continuous controller design and discretized linearization is still preferred because the linear math calculation without exponential functions is easier to implement.

For the PM machine drive at high speed, considerable mechanical friction losses might appear if ball bearings are used to support the machine rotating component. Besides, the ball bearing lifetime significantly reduces for long time high speed operation [22]. To minimize high speed friction losses, magnetic bearings with the non-contact support of machine rotor is developed instead of ball bearings with mechanical contact. In general, magnetic bearings can be realized based on the radial force generated by separated coils [23], [24] or integrated coils in the stator [25], [26]. The machine with integrated stator coils, e.g. bearingless machine, has the size advantage which is suited for moving motion systems. However, the insufficient power density is the primary issue [26]. In addition, the magnetic bearing is able to manipulate the radial force for the rotor vibration compensation [24]. It further improves the rotor dynamic strength for high speed machine drives.

This paper concentrates on the improvement of high speed PM machine FOC under insufficient sample frequency. Considering the digital implementation, the performance of FOC regulated sinusoidal currents significantly degrades as the speed increases. To overcome this limitation, three conventional discrete-time linearization methods are systematic evaluated to find a best suited digital current controller for high speed FOC drive. Although several digital machine controllers have reported at this time [9], [12], [13], [19]–[21], there are very few papers related to the evaluation of standard discrete-time linearization methods and possible improvement. In this paper, the linearization based on forward difference, backward difference and bilinear approximation are all compared. It is shown that either forward difference or bilinear approximation can maintain the FOC at $f_{sample}/f_e \approx 5$ if the voltage delay and inductance cross-coupling are fully considered. However when the controller bandwidth is high, the forward difference design results in the stability issue. By contrast, the bilinear design achieves the reduced effect on the controller bandwidth as speed increases. More importantly, the digital controller using direct design with nonlinear functions is also developed for the performance comparison. In this paper, a 8-pole interior PM machine with 32krpm maximum speed whereby $f_{sample}/f_e = 4.7$ is experimentally tested to compare drive performance among different controllers. This paper includes the design guidance of high speed FOC for machines with different time constants.

## II. DIGITAL CONTROLLER DESIGN
This section explains the current controller design for high speed drive. Three approximation methods are used to realize the digital controller. The influence of controller bandwidth and operating speed are analyzed.

### A. COMPLEX CURRENT CONTROLLER
Fig. 1 shows the signal flowchart of complex current controller in continuous-time [14]. In this figure, a salient PM machine is considered, where is the machine resistance, is the magnet flux, and $\omega_e = 2\pi f_e$ is the rotor speed. 1/s represents the integration in Laplace S-domain. In addition, $V_d^*/V_q^*$, and $i_d/i_q$ are respectively machine dq voltage commands and measured currents. The superscript * denotes the command signal generated by controllers.
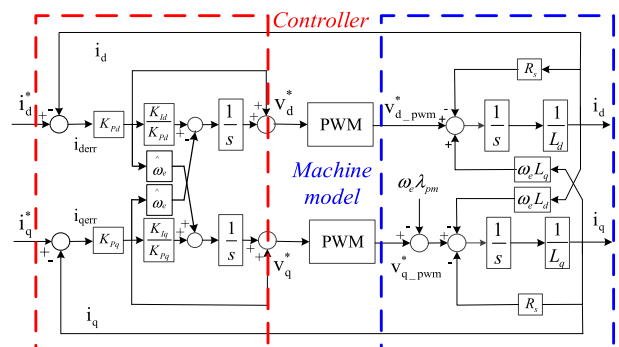


**FIGURE 1.** dq current controller design in continuous-time.

It is noted that the inductance cross-coupling occurs on dq machine model where the differential equation is given by

$$\begin{bmatrix} v^*_{d\_pwm}(t) \\ v^*_{q\_pwm}(t) \end{bmatrix} = \begin{bmatrix} R_s+pL_d & -\omega_e L_q \\ \omega_e L_d & R_s+pL_q \end{bmatrix} \begin{bmatrix} i_d(t) \\ i_q(t) \end{bmatrix} + \begin{bmatrix} 0 \\ \omega_e\lambda_{pm} \end{bmatrix}$$
(1)

In (1), $v^*_{d\_pwm}/v^*_{q\_pwm}$ are dq voltage commands after PWM as seen in Fig. 1, and p=d/dt is the differential operator. It is noted that the simultaneous equation in (1) can be organized by a single complex equation in (2) to easily illustrate the cross-coupling effect.

$$V^*_{dq\_pwm}(t) = R_s I_{dq}(t) + (p + j\omega_e)\,\lambda_{dq}$$
$$\lambda_d(t) = L_d i_d(t) + \lambda_{pm} \text{ and } \lambda_q(t) = L_q i_q(t) \quad (2)$$

In (2), $v^*_{dq\_pwm} = v^*_{d\_pwm} + v^*_{q\_pwm}$ and $I_{dq} = i_d + j\,i_q$ are all complex variables. In addition, $\lambda_{dq} = \lambda_d + j\,\lambda_q$ are complex variables of dq flux linkages. Under this effect, the S-domain transfer function between $I_{dq}(s)$ and $v^*_{dq\_pwm}(s)$ is derived by

$$\text{d-axis:} \quad \frac{I_d(s)}{V^*_{d\_pwm}(s)} = \frac{1/L_d}{s + \left(j\omega_e + R_s/L_d\right)}$$

$$\text{q-axis:} \quad \frac{I_q(s)}{V^*_{q\_pwm}(s)} = \frac{1/L_q}{s + \left(j\omega_e + R_s/L_q\right)} \quad (3)$$

In (3), the EMF voltage drop $\omega_e\lambda_{pm}$ is assumed as an external disturbance considering the ideal current regulation. It is found that a speed dependent term appears as $\omega_e$ increases, leading to the transient oscillation. This speed dependent term can be compensated based on the complex current controller, as shown from the red box in Fig. 1. The corresponding transfer function is given by

$$\text{d-axix:} \quad \frac{V^*_d(s)}{I^*_d(s) - I_d(s)} = K_{pd}\frac{s + \left(j\hat\omega_c + K_{Id}/K_{P_d}\right)}{s}$$

$$\text{q-axix:} \quad \frac{V^*_q(s)}{I^*_q(s) - I_q(s)} = K_{pd}\frac{s + \left(j\hat\omega_c + K_{Iq}/K_{P_q}\right)}{s} \quad (4)$$

where $K_{Pd}/K_{Pq}$ and $K_{Id}/K_{Iq}$ are proportional and integral gains of complex current controller, and $\hat\omega_e$ is the estimated rotor frequency. The superscript ^ denotes the estimated variable. In general, these controller gains can be designed based on (5).

$$\text{d-axis: } K_{Pd} = K_{BW}\hat L_d \text{ and } K_{Id} = K_{BW}\hat R_s$$
$$\text{q-axis: } K_{Pq} = K_{BW}\hat L_q \text{ and } K_{Iq} = K_{BW}\hat R_s \quad (5)$$

where $\hat L_d/\hat L_q$ are respectively estimated d- and q-axis inductances, $\hat R_s$ is the estimated resistance and is the controller gain. Based on the design in (5), the machine speed dependent pole in (3) can be cancelled by the controller zero. It is noted that machine resistance and inductance parameters are required to achieve the pole/zero cancellation. Under this effect, the relationship between $I^*_{dq}(s)$ commands and $I_{dq}(s)$

outputs are equivalent to two independent first-order systems, as given by

$$\text{d-axis:} \; \frac{I_d(s)}{I^*_d(s)} = \frac{K_{BW}}{s + K_{BW}} \text{ and q-axis:} \; \frac{I_q(s)}{I^*_q(s)} = \frac{K_{BW}}{s + K_{BW}}$$
(6)

In (6), the overall current controller bandwidth can be designed based on. Assuming the perfect parameter estimation, the inductance nonlinear cross-coupling is decoupled, leading to a stable FOC drive at high speed.

### B. DISCRETE-TIME MACHINE MODEL

This part analyzes the digital implementation issues on the current controller. Assuming the PWM in Fig. 1 is modeled by a ZOH converter, the continuous machine model based on differential equations in (1) can be transformed to the discretized difference equations in (7) [9].

$$I_{dq}(k) = e^{-\left(\frac{R_s}{\Sigma L}+j\omega_e\right)T_s} I_{dq}(k-1) + \frac{e^{-j\omega_e T_s} - e^{-\left(\frac{R_s}{\Sigma L}+j\omega_e\right)T_s}}{R_s}$$

$$\times \left\{ V^*_{dq\_pwm}(k-1) - \frac{R_s}{R_s + j\omega_e \sum L} \right.$$

$$\left. \times \frac{e^{j\omega_e T_s} - e^{-\frac{R_s}{\Sigma L}T_s}}{1 - e^{-\frac{R_s}{\Sigma L}T_s}} j\omega_e\lambda_{pm}(k-1) \right\} \quad (7)$$

where $T_s = 1/f_{sample}$ is the controller sample time, and k and (k-1) represent the current and last sample step for difference equations. In (7), it is important to note that d- and q-axis inductance $L_d$, and $L_q$, are simplified by the average inductance $\Sigma L = (L_d + L_q)/2$ in order to develop the complex difference equation for the stability analysis [9]. Considering PM machines with high saliency ratios, the cross-coupled discrete-time state equations developed in [20] are recommend for the analysis. However, the analytical insight might be difficult to identify on these nonlinear cross-coupled equations.
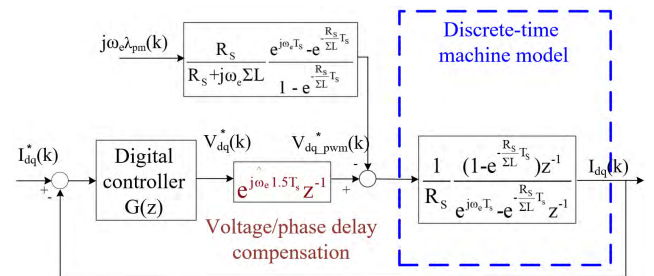


**FIGURE 2.** Signal flowchart of the machine model in discrete-time considering the ZOH.

Fig. 2 illustrates the signal process of discrete-time machine model in Z-domain. Due to the influence of ZOH, the linear inductance cross-coupling component $j\omega_e\Sigma L$ changes to a nonlinear exponential component. $e^{-j\omega_e T_s}$. In addition, ZOH also results in 1.5 $T_s$ delay per sample instant during the park transformation [10], [11].
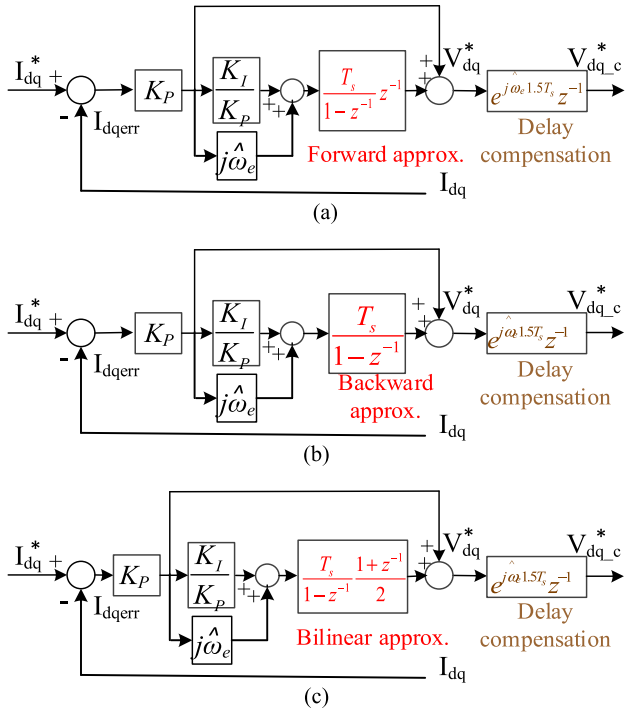
**FIGURE 3.** The realization of digital controller G(z) in Fig. 2 based on (a) forward difference and (b) backward, and (c) bilinear approximation.

Both the influence of cross-coupling and phase delay increase as $f_{sample}/f_e$ decreases. These two issues lead to the FOC stability issue at high speed.

### C. DIGITAL CONTROLLER APPROXIMATION

This part investigates the digital controller design based on the digital linearization of continuous complex controller in Fig. 1. Assuming that the sample time $T_s$ is sufficiently small ($T_s \approx 0$), the nonlinear sample impulse response $z = e^{sT_s}$ can be simplified by three linear math functions, as given by

$$z = e^{sT_s} \approx 1 + sT_s \text{ where } sT_s \approx 0 \quad (8)$$

$$z = \frac{1}{e^{-ST_s}} \approx \frac{1}{1 - sT_s} \text{ where } -sT_s \approx 0 \quad (9)$$

$$z = \frac{e^{sT_s/2}}{e^{-sT_s/2}} \approx \frac{1 + sT_s/2}{1 - sT_s/2} \text{where } -sT_s/2 \approx 0 \quad (10)$$

(8), (9) and (10) represent the linear approximation respectively based on forward difference, backward difference and bilinear transformation. Under these assumptions, the digital controller G(z) in Fig. 2 can be designed by applying these approximations into (4).

Fig. 3 illustrates the Z-domain transfer function of G(z) using three approximations. In Fig. 3(a), the forward difference is realized. On the basis, the digital integration is linearized by an accumulation $T/(1 - Z^{-1})$ pulse one-step voltage delay $Z^{-1}$. It is noted that additional voltage and phase delay compensation is added to resolve the influence of ZOH on the park transformation [10], [11]. In addition, the digital controller gains $K_P$, and $K_I$, are designed based

on (5) where the average inductance $\Sigma\hat{L} = (\hat{L}_d + \hat{L}_q)/2$ is used instead of $\hat{L}_d$ and $\hat{L}_q$.

By contrast, Fig. 3(b) introduces the controller design using backward difference. Different to forward in (a), the digital integration is simply linearized by $T/(1 - Z^{-1})$. Finally, Fig. 3(c) shows the controller using bilinear approximation. On this basis, bilinear is an average of the forward difference in (8) and backward in (9). Due to an additional average process $(1 - z^{-1})/2$, the bilinear might achieve the most accurate linearization performance among three approximations in Fig. 3.

However for the actual discrete-time machine model in Fig. 2, the continuous inductance cross-coupling is also changed from linear function $j\omega_e\Sigma L$ to a nonlinear $e^{-j\omega eTs}$. Under this effect, the overall current regulator might not equivalent to a first-order system similar to (6) in continuous time. More importantly, the influence of $e^{-j\omega eTs}$ increases as speed increases, leading to stability issues on the high speed FOC drive.

### III. CLOSED-LOOP SYSTEM ANALYSIS

This section investigates the dynamic response of high speed drive among three digital controllers in Fig. 3. The root locus migration is used to analyze the closed-loop system stability. Both the influence of controller bandwidth and operating frequency on three closed-loop systems are compared to find a suited high speed controller. It is noteworthy that for the proposed root locus analysis, an ideal current regulation without SVPWM is considered. In addition, the digital implementation software delay and current sensing noises are all neglected for simplicity. Under this effect, the simulation performance might be better than the actual performance obtained by the experiment. However since the influences of SVWPM, software delay and current noises on three digital controllers are the same, the performance difference should be the same between simulation and experiment.

Considering the discrete-time machine model in (7), the equivalent Z-domain transfer function between output $I_{dq}(k)$ and input $v^*_{dq\_pwm}(k)$ is given by

$$\frac{I_{dq}(z)}{V^*_{dq\_pwm}(z)} = \frac{1}{R_s}\left(e^{-j\omega_eT_s} - e^{-\frac{R_s}{\Sigma L}T_s}e^{-j\omega_eT_s}\right)$$

$$\times \frac{1}{z - e^{-\frac{R_s}{\Sigma L}T_s}e^{-j\omega_eT_s}} \quad (11)$$

where a speed dependent pole appears at $z$ $Z = e^{-j\omega eTs}e^{-(R_sT_s/\Sigma L)}$. For the MCU with the sample time around $50\sim 100$msec, this pole is close to the unit circle where $|z| \approx 1$. By applying the forward difference in Fig. 3(a), the corresponding controller transfer function is shown by

$$\frac{V^*_{dq}(z)}{I^*_{dq}(z) - I_{dq}(z)} = K_{BW}\frac{\sum\hat{L}z + j\hat{\omega}_e\sum\hat{L} - \sum\hat{L} + \hat{R}_sT_s}{z - 1}$$

$$(12)$$

where the inductance cross-coupling is expected to decouple in continuous-time based on the design of controller gains $K_P$,
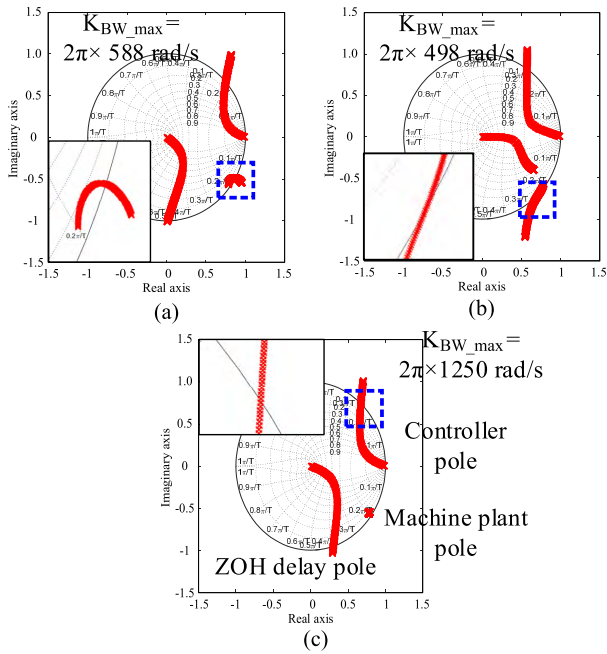
**FIGURE 4.** Closed-loop pole migration as the change of controller gain $K_{BW}$: (a) Forward difference, (b) backward difference, and (c) bilinear approximation ( $f_e$ = 1kH, $f_{sample}$/$f_e$ = 10, $L_d$ = 0.786mH, $L_q$ = 1.052, $\Sigma L$ = 0.919mH and $R_S$ = 0.3 $\Omega$).



**FIGURE 5.** Closed-loop pole migration as the change of rotor frequency $f_e$: (a) Forward difference, (b) backward difference, and (c) bilinear approximation ($K_{BW}$ = 2$\Pi$ × 160 rad/s, $f_{sample}$/$f_e$ = 10, $L_d$ = 0.786mH, $L_q$ = 1.052mH, $\Sigma L$ = 0.919mH and $R_S$ = 0.3 $\Omega$).

and $K_I$. In (12), a controller pole is at z=1. Besides as seen in Fig. 3, a third pole occurs on z=0 due to the one step voltage delay compensation of ZOH. By combining the controller model in (12), delay compensation in Fig. 3, and the machine model in (11), the overall transfer function of current regulation is developed by

$$\frac{I_{dq}(z)}{I_{dq}^*(z)} = \frac{G_{open}(z)}{1 + G_{open}(z)} \qquad (13)$$

In (13), $G_{open}(Z)$ represents the open-loop transfer function for the root locus analysis. It is shown to be

$$G_{open}(z)$$

$$= K_{BW} \left\{ \frac{\sum \hat{L}z + j\hat{\omega}_e \sum \hat{L} - \sum \hat{L} + \hat{R}_s}{z - 1} \frac{e^{j\omega_e 1.5T_s}}{z} \right.$$

$$\left. \times \frac{1}{R_s} \left( e^{-j\omega_e T_s} - e^{-\frac{R_s}{\Sigma L}T_s}e^{-j\omega_e T_s} \right) \frac{1}{Z - e^{-\frac{R_s}{\Sigma L}T_s}e^{-j\omega_e T_s}} \right\}$$

$$(14)$$

where the overall current regulation bandwidth can be determined based on a single controller gain $K_{BW}$. Similar closed-loop transfer functions can be derived for digital controllers using backward difference and bilinear approximation.

### A. STABILITY ANALYSIS AT DIFFERENT BANDWIDTHS

Fig. 4 compares the pole migration of three closed-loop systems as the increase of controller gain $K_{BW}$. In this simulation, the rotor frequency $f_e$ is set at 1kHz where $f_{sample}$/$f_e$ = 10. Unlike the continuous system in (6), the discrete-time current regulation is no longer equivalent to a 1st-order system. The under-damped oscillation appears
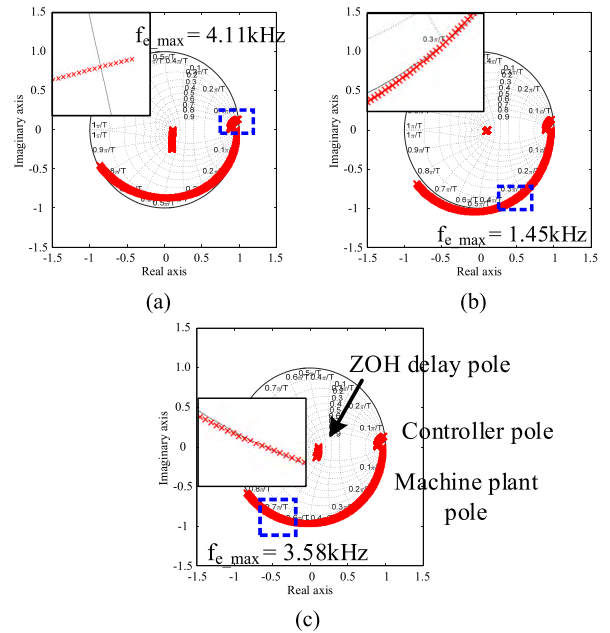
as $K_{BW}$ increases. More importantly, the current regulation eventually becomes unstable once $K_{BW}$ is larger than a certain amount of value, as seen from the blue frame in Fig 4.

Comparing the closed-loop stability among three controllers in Fig. 4, the backward in (b) results in the smallest stable $K_{BW}$ where the overall bandwidth is below 498 Hz. It is observed that the machine plant pole $z = e^{-j\omega eTs}e^{-(R_sT_s/\Sigma L)}$ quickly moves to the outside of unit circle. A pure digital integration without any modification in Fig. 3(b) might be the primary issue on backward difference. By contrast for forward difference in Fig. 4(a), the maximum stable bandwidth can improve to 588Hz by adding one step delay on the integration. More importantly, the bilinear approximation in Fig. 4(c) results in the highest bandwidth at 1.25kHz. Because of additional average process during the digital integration, the machine plant pole at z = $e^{-j\omega eTs}e^{-(R_sTs/L_{dq})}$ always keeps stable, leading to the best dynamic response.

### B. STABILITY ANALYSIS AT DIFFERENT SPEEDS

Instead of controller gain $K_{BW}$ analysis, the closed-loop pole migration as the increase of rotor frequency is also evaluated in Fig. 5. In this simulation, the controller bandwidth is set at 160Hz to analyze the system stability at different $f_e$. Because of the non-perfect inductance cross-coupling decoupling, the machine plant pole moves along the boundary of unit circle among three linearization methods. It is expected the oscillation property increases as $f_e$ increases.

Comparing the pole migration among three closed-loop systems, the stability using backward difference in (b) significantly degrades as increases. The maximum rotor frequency is limited at $f_e$ = 1.45 kHz where $f_{sample}$/$f_e$ = 6.9.

However for the forward difference in (a), the maximum rotor frequency increases to $f_e = 4.11$ kHz where $f_{sample}/f_e = 2.4$. More importantly, the machine plant pole maintains within unit circle as $f_e$ increases. The additional one step delay for the digital integration is the primary advantage to compensate the inductance cross-coupling with the phase lagging property. Besides, the maximum rotor frequency slightly decreases to $f_e = 3.58$ kHz where $f_{sample}/f_e = 2.8$ using the bilinear approximation in (c).
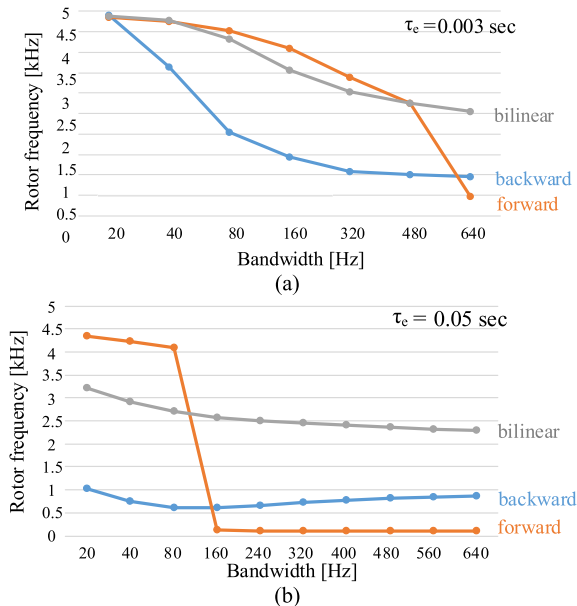


**FIGURE 6.** Rotor frequency versus the controller bandwidth for two PM machines with (a) time constant 0.003 sec and (b) 0.05 sec.

## C. COMPARISON OF DIFFERENT MACHINES

It is important to note that the controller linearization design strongly depends on machine parameters. For the root locus analysis in Fig. 4 and 5, an interior PM machine with an electric time constant $\tau_e = \Sigma L/R_s = 0.003$sec is selected. Considering various high speed PM machines, it is worth to analyze the controller performance for machines with different. Fig. 6 compares the maximum rotor frequency versus the control bandwidth for two machines with (a) $\tau_e = 0.003$ and (b) $\tau_e = 0.05$sec. In this figure, the rotor frequency is obtained based on the root locus analysis considering the critical stable point in Fig. 5 blue frame.

In general for a machine with small $\tau_e$ in Fig. 6(a), e.g. low inductance machine, the linear approximation can achieve the better high speed drive performance comparing to the machine with big in $\tau_e$ (b). Besides, the forward difference in (a) results in the highest $f_e$ when the controller bandwidth is below 480 Hz. However when the bandwidth is beyond 480Hz, the forward difference performance quickly degrades. More importantly, the performance difference between forward and bilinear is negligible at low controller bandwidths.

Considering a machine with big $\tau_e$ in Fig. 6, the forward shows the lowest rotor operating frequency once the

**TABLE 1.** Test machine characteristics.

| Characteristics | Values |
|---|---|
| Rotor poles | 8 pole |
| Rated torque | 0.41 Nm |
| Rated current | 9 A |
| Rated/Maximum speed | 6krpm/32krpm |
| Resistance | 0.3Ω |
| Inductance | 0.786mH (d-axis)/1.052mH(q-axis) |
| DC bus voltage | 150 V |
| PWM frequency | 10 kHz |

bandwidth is higher than 80Hz. As seen in (b), a sharp drop occurs on forward difference. The specific pole migration of z=1 outside unit circle in Fig. 5(a) might be the primary issue to cause this significantly degraded performance. By contrast, the bilinear approximation is robust for the big $\tau_e$ machine though the maximum $f_e$ slightly decreases as the bandwidth increases. Comparing Fig. 6(a) and (b), it is concluded that the digital controller using the bilinear approximation is suited for high speed drives especially for big $\tau_e$ PM machines.

## IV. EXPERIMENTAL RESULTS

A 8-pole interior PM machine with the maximum speed at 32krpm ($f_e = 2.13$kHz) is built for the high speed FOC drive using different controller design methods. The PWM frequency is set at 10 kHz synchronizing to the current sample frequency. In this paper, FOC with only q-axis current is used to evaluate controller discretized effects excluding the flux weakening for simplicity. Key machine drive characteristics are listed in Table 1. It is noted that in this paper, the EMF-based sensorless drive in [27] is developed for the position and speed estimation to realize the high speed FOC. In order to verify the sensorless estimation accuracy, a magnetic encoder is installed for only the comparison of estimated position and speed. Fig. 7 shows (a) the test PM machine rotor configuration, and (b) the drive test bench. A hysteresis dyno is coupled with the test machine to apply the torque load. All sensorless drive algorithms are implemented in a 32-bit microcontroller, TI-TMS320F28069.
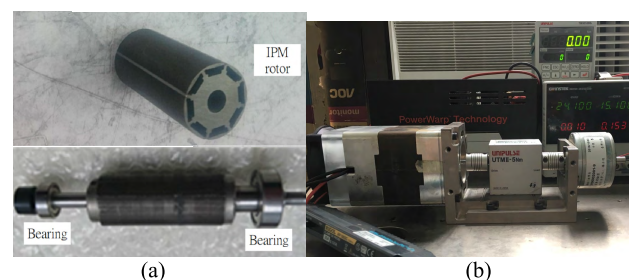


**FIGURE 7.** Photograph of (a) PM machine rotor and (b) drive test bench.

## A. CONTROLLER PERFORMANCE AT DIFFERENT BANDWIDTHS

This part compares the high speed drive performance among three approximation methods. Different controller bandwidths are evaluated to verify simulation results in Fig. 4.
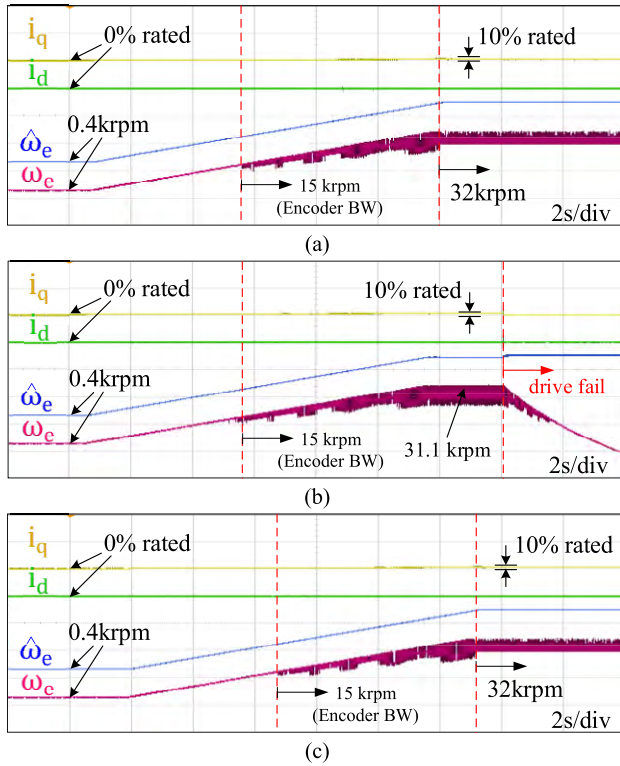
**FIGURE 8.** Machine acceleration from 0.4kprm to 32krpm where the controller design is based on (a) forward difference, (b) backward and (c) bilinear approximation (25Hz bandwidth and no load).



**FIGURE 9.** Machine acceleration from 0.4kprm to 20krpm where the controller design is based on (a) forward difference, (b) backward and (c) bilinear approximation (40Hz bandwidth and no load).

Fig. 8 shows the drive acceleration from 0.4krpm to 32krpm ($f_e$ = 2.13kHz and $f_{sample}$ /$f_e$ = 4.69) without load. In this test, the controller bandwidth is designed at 25Hz to evaluate the FOC at low bandwidth. Time-domain waveforms of $i_q$, $i_d$ , estimated speed $\hat{\omega}_e$ and measured speed are respectively shown. The closed-loop speed control is implemented based on the feedback of estimated $\hat{\omega}_e$ and $\hat{\theta}_e$. The measured is shown for comparison only. As seen in Fig. 8, the controller using backward difference results in the worst drive performance where the maximum speed is limited at 31.1krpm. By contrast, both forward in (a) and bilinear in (c) maintain the drive stability at 32krpm maximum speed where $f_{sample}$ /$f_e$ = 4.69. It is found that considerable noises are observed in measured when the speed is beyond 15krpm due to the insufficient encoder sensing bandwidth.

Fig. 9 shows the same experiment while the controller bandwidth is increased to 40Hz. At this bandwidth, all three FOC drives fail to reach 32krpm maximum speed. More importantly, the controller using backward difference in (b) still results in the worst performance whereby $f_{sample}$ /$f_e$ = 9.67. among three approximations. On the other hand, the forward in (a) and bilinear in (c) improves the operating speed to $f_{sample}$ /$f_e$ = 8.02. By comparing Fig. 8 and Fig. 9, it is concluded that the backward difference has the limitation for high speed FOC. Comparing to simulation results, it is important that maximum speeds among three digital controllers all degrade from experiment. For actual machine drives, additional implementation issues must con-
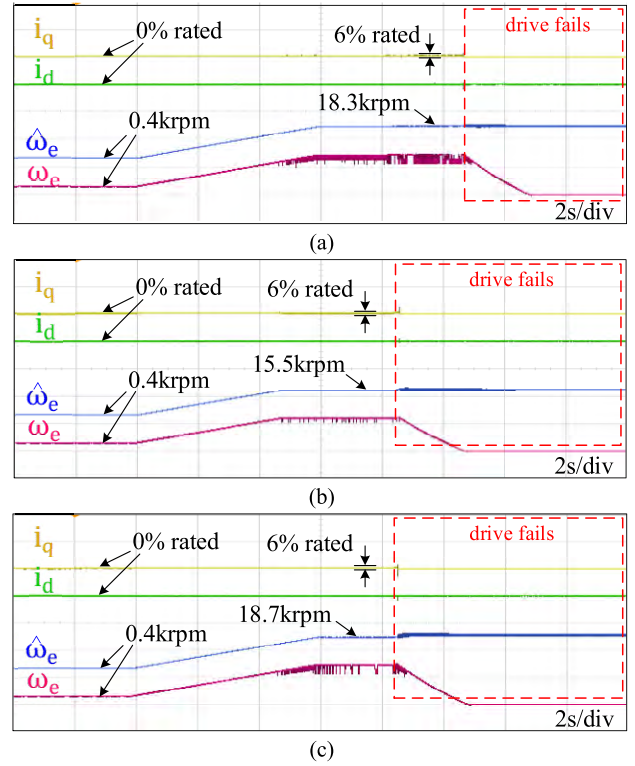
sidered, e.g. PWM switching, software calculation delay and current sensing, software. These limitations are neglected for the root locus simulation in section III for simplicity. Nevertheless, the performance difference is consistent among three linearized controllers under same controller bandwidths.

### B. SPEED CONTROL UNDER LOAD

This part evaluates the closed-loop speed control under a step load. In this test, the machine speed is maintained at 15krpm ($f_e$ = 1kHz and $f_{sample}$ /$f_e$ = 10) with 25Hz bandwidth. A 120% step torque load is applied by the dyno. Fig. 10 shows the performance comparison among three digital controllers. In this figure, time-domain waveforms of $i_q$, $i_d$, $\hat{\omega}_e$ and $\omega_e$ are respectively shown. Similar to the acceleration experiment at part A, the backward difference in (b) is not able to maintain 15krpm speed under 120% step load. By contrast, the forward and bilinear successfully maintain the speed at 15krpm under load. As mentioned in Fig. 5, two closed-loop poles move toward the unit circle at high $f_e$. More importantly, the closed-loop stability greatly degrades at high $f_e$ using the backward difference linearization. Under this effect, the backward difference leads to the stability issue considering the parameter variation once load increases. It is shown that the experimental result is consistent with the analysis in Fig. 5, where the backward difference contains the stability issue at high speed. This linearization design is not recommended for high speed FOC drive.
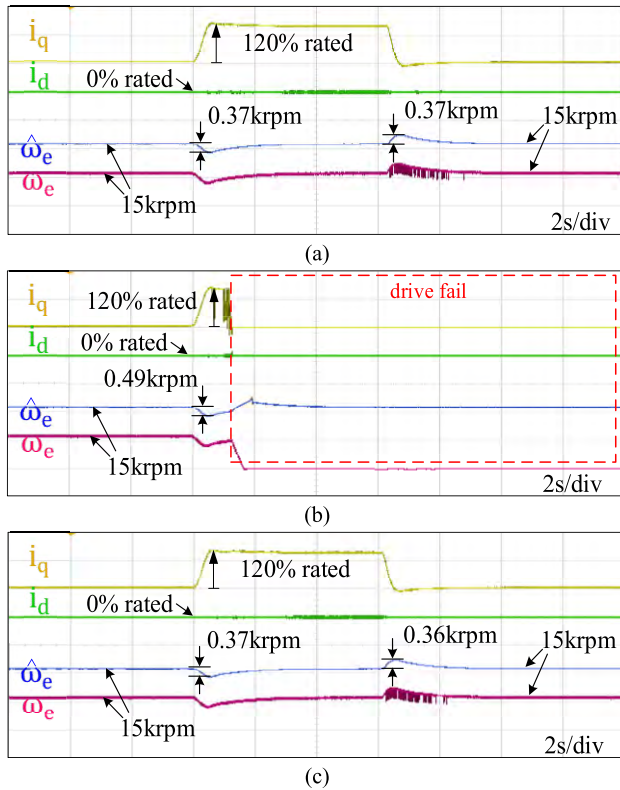
(a)


(b)


(c)

**FIGURE 10.** Closed-loop speed control under a step load where the controller is using (a) forward difference, (b) backward and (c) bilinear approximation (25Hz bandwidth and 15krpm speed).

## C. ACCELERATION UNDER LOAD

This part evaluates the drive acceleration under two different drag loads. Because of the maximum speed limitation on the hysteresis dyno at 15krpm, an impeller is attached on the machine rotor shaft to simulate the fan operation. At this part, the controller bandwidth is set at 25Hz similar to the condition in Fig. 10. The backward difference is excluded due to its worst performance at high speed.

Fig. 11 shows the drive acceleration under a low drag load. Both the forward in (a) and bilinear in (b) achieve the same performance where 47% rated current is used at 32krpm and $f_{sample}/f_e = 4.69$. It is important to note that FOC quickly loses the stability if the voltage delay is not compensated for these two controllers.

Fig. 12 shows the same acceleration experiment while a higher drag load is applied. In this experiment, the controller using the directly digital design developed in [9] is also added in (c) to compare the acceleration performance under heavy load. It is found that both the forward in (a) and bilinear in (b) eventually fail when the rated current is around 90% at 29krpm speed. Although the voltage delay is compensated, the non-perfect inductance cross-coupling decoupling in discrete-time analyzed in Fig. 5 is the primary issue on these two linearization methods. By contrast in (c), the controller using the directly digital design still maintains the stability at 148% rated current under 32kprm maximum speed.
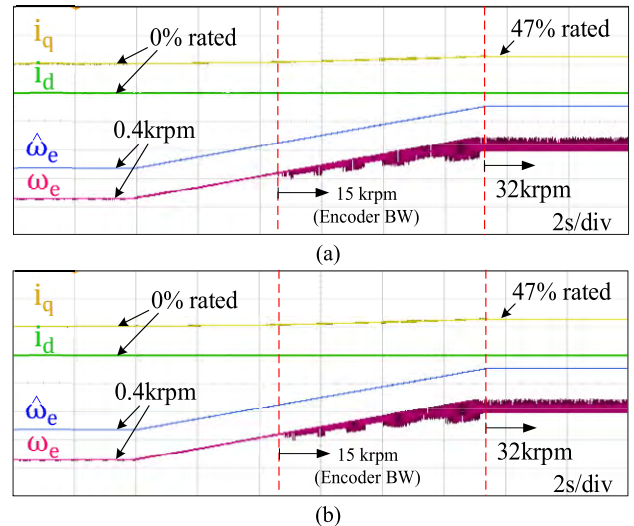

(a)


(b)

**FIGURE 11.** Machine acceleration from 0.4kprm to maximum 32krpm where the controller design is (a) forward and (b) bilinear (25Hz bandwidth and low drag load).
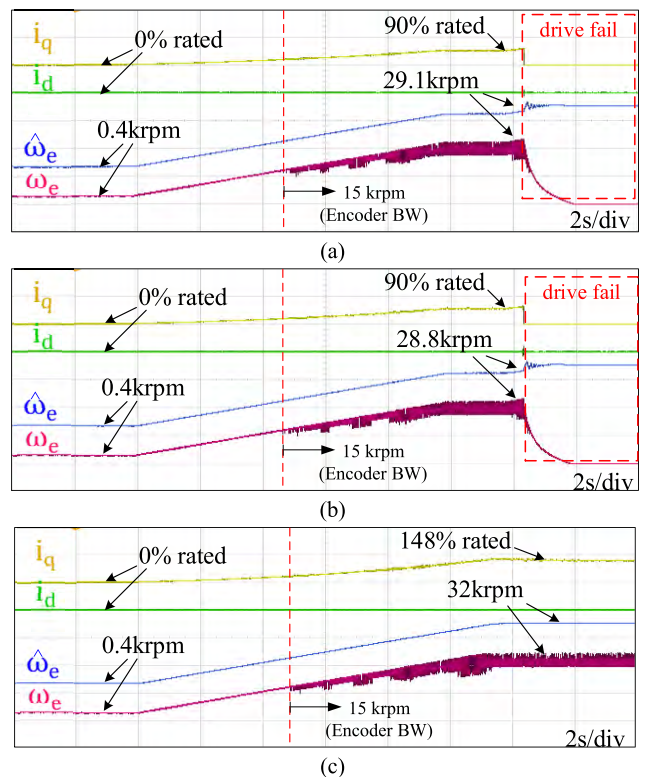

(a)


(b)


(c)

**FIGURE 12.** Machine acceleration from 0.4kprm to maximum 32krpm where the controller design is using (a) forward, (b) bilinear and (c) direct digital design (25Hz bandwidth and high drag load).

Nevertheless, this controller contains several nonlinear exponential functions which might not be suited for FOC at low cost. Table 2 compares the algorithm implementation requirement among different controllers using forward, bilinear and direct design. In this table, all the used math functions, memory sizes and calculation times are compared. It is shown

**TABLE 2.** Algorithm implementation comparison.

| Property | Forward | | Bilinear | | Direct Design | |
|---|---|---|---|---|---|---|
| | # | CPU Cycles | # | CPU Cycles | # | CPU Cycles |
| 32-bit Summation | 6 | 6 | 8 | 8 | 4 | 4 |
| 32-bit Multiplication | 4 | 24 | 4 | 24 | 10 | 60 |
| 32-bit Division | 0 | 0 | 2 | 126 | 2 | 126 |
| Exponential Function | 0 | 0 | 0 | 0 | 4 | 380 |
| Calculation Period (%) | | 2.85% | | 3.36% | | 5% |
| 32-bit Variables | | 7 | | 7 | | 9 |
| Stability | | Low | | Low | | High |

Note: All algorithms are implemented in TI TMS320F28069 processor
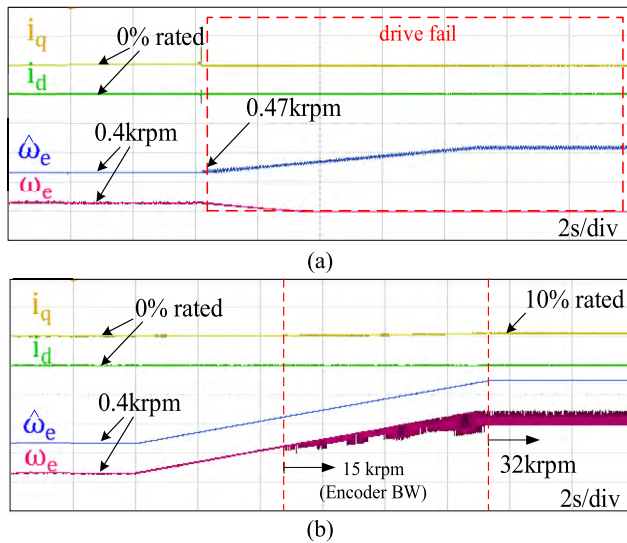


(a)



(b)

**FIGURE 13.** Inductance sensitivity test: Machine acceleration to 32krpm when the (a) bilinear approximation and (b) direct design is implemented (25Hz bandwidth and $\hat{L}_q = 2L_q$).

that the direct design requires four nonlinear exponential functions for d- and q-axis current control, adding 380 more cpu cycles. Under this effect, the overall calculation period is almost twice comparing to the forward difference. This relatively complicated algorithm can be a challenge for the implementation using low cost MCU.

### D. PARAMETER SENSITIVITY

This part evaluates the influence of inductance variation on the high speed FOC when the controller is designed based on bilinear approximation and directly digital design. Fig. 13 analyzes the machine acceleration with the inductance estimation error. The estimated q-axis inductance $\hat{L}_q$ is designed intentionally equal to $2L_q$ considering the inductance saturation at high speed. Because the inductive voltage drops increases as speed increases, the inductance error causes the stability issue at high speed.

As seen in (a) using the bilinear approximation, the FOC quickly fails when the drive accelerates to 0.47krpm if $\hat{L}_q = 2L_q$. The same inductance sensitive issue is also observed for the controller using forward and backward difference. By contrast in (b) using direct design, the FOC can reach the maximum speed at 32krpm under the same inductance error. Based on this experiment, it is concluded that

the real-time inductance estimation must be applied for FOC using linearization methods. Otherwise, the directly digital design should be applied when the PM machine contains the visible inductance saturation. Finally, it is also noted that the resistance variation results in the negligible effect on FOC using linearization methods based on other experimental results.

## V. CONCLUSIONS
Key conclusions are summarized as follows:

- The linearization design based on forward difference and bilinear approximation might be able to maintain the FOC stability at $f_e = 2.13$kHz and $f_{sample}/f_e = 4.69$ if the inductance parameter is perfectly estimated.
- The current controller using the backward difference approximation shows the worst high speed FOC performance. The pure digital integration without any delay compensation in Fig. 3(b) is the primary issue.
- The controller using the directly digital design has advantages for high speed FOC under heavy load and inductance estimation error. However, the MCU memory and bandwidth should be considered in order to realize several exponential functions real-time.

### REFERENCES
[1] S. Silber, J. Sloupensky, P. Dirnberger, M. Moravec, W. Amrhein, and M. Reisinger, "High-speed drive for textile rotor spinning applications," *IEEE Trans. Ind. Electron.*, vol. 61, no. 6, pp. 2990–2997, Jun. 2014.

[2] C. Gu, X. Wang, X. Shi, and Z. Deng, "A PLL-based novel commutation correction strategy for a high-speed brushless DC motor sensorless drive system," *IEEE Trans. Ind. Electron.*, vol. 65, no. 5, pp. 3752–3762, May 2018.

[3] C. Zwyssig, S. D. Round, and J. W. Kolar, "An ultrahigh-speed, low power electrical drive system," *IEEE Trans. Ind. Electron.*, vol. 55, no. 2, pp. 577–585, Feb. 2008.

[4] L. Schwager, A. Tuysuz, C. Zwyssig, and J. W. Kolar, "Modeling and comparison of machine and converter losses for PWM and PAM in high-speed drives," *IEEE Trans. Ind. Appl.*, vol. 50, no. 2, pp. 995–1006, Mar. 2014.

[5] B. Song, L. Xu, and X. Lu, "A comparative study on Tustin rule based discretization methods for fractional order differentiator," in *Proc. 4th IEEE Int. Conf. Inf. Sci. Technol.*, Apr. 2014, pp. 515–518.

[6] D. P. Marčetić, I. R. Krčmar, M. A. Gecić, and P. R. Matić, "Discrete rotor flux and speed estimators for high-speed shaft-sensorless IM drives," *IEEE Trans. Ind. Electron.*, vol. 61, no. 6, pp. 3099–3108, Jun. 2014.

[7] F. D. Freijedo *et al.*, "Tuning of synchronous-frame pi current controllers in grid-connected converters operating at a low sampling rate by MIMO root locus," *IEEE Trans. Ind. Electron.*, vol. 62, no. 8, pp. 5006–5017, Aug. 2015.

[8] D. W. Clarke and S. P. Maslen, "Discretising controllers with slow sampling," *IET Control Theory Appl.*, vol. 1, no. 3, pp. 624–635, May 2007.

[9] H. Kim, M. W. Degner, J. W. Guerrero, F. Briz, and R. D. Lorenz, "Discrete-time current regulator design for AC machine drives," *IEEE Trans. Ind. Appl.*, vol. 46, no. 4, pp. 1425–1435, Jul./Aug. 2010.

[10] B.-H. Bae and S.-K. Sul, "A compensation method for time delay of full-digital synchronous frame current regulator of PWM AC drives," *IEEE Trans. Ind. Appl.*, vol. 39, no. 3, pp. 802–810, May 2003.

[11] D. Q. Truong, K. K. Ahn, and N. T. Trung, "Design of an advanced time delay measurement and a smart adaptive unequal interval grey predictor for real-time nonlinear control systems," *IEEE Trans. Ind. Electron.*, vol. 60, no. 10, pp. 4574–4589, Oct. 2013.

[12] G. Zhang, G. Wang, D. Xu, and Y. Yu, "Discrete-time low-frequency-ratio synchronous-frame full-order observer for position sensorless IPMSM drives," *IEEE J. Emerg. Sel. Topics Power Electron.*, vol. 5, no. 2, pp. 870–879, Jun. 2017.

[13] S. N. Vukosavic, L. S. Peric, and E. Levi, "Digital current controller with error-free feedback acquisition and active resistance," *IEEE Trans. Ind. Electron.*, vol. 65, no. 3, pp. 1980–1990, Mar. 2018.

[14] F. Briz, M. W. Degner, and R. D. Lorenz, "Analysis and design of current regulators using complex vectors," *IEEE Trans. Ind. Appl.*, vol. 36, no. 3, pp. 817–825, May/Jun. 2000.

[15] X. Sun, L. Chen, H. Jiang, Z. Yang, J. Chen, and W. Zhang, "High-performance control for a bearingless permanent-magnet synchronous motor using neural network inverse scheme plus internal model controllers," *IEEE Trans. Ind. Electron.*, vol. 63, no. 6, pp. 3479–3488, Jun. 2016.

[16] X. Sun, Z. Shi, L. Chen, and Z. Yang, "Internal model control for a bearingless permanent magnet synchronous motor based on inverse system method," *IEEE Trans. Energy Convers.*, vol. 31, no. 4, pp. 1539–1548, Dec. 2016.

[17] X. Sun *et al.*, "MPTC for PMSMs of EVs with multi-motor driven system considering optimal energy allocation," *IEEE Trans. Magn.*, to be published.

[18] B. H. Kenny and R. D. Lorenz, "Stator- and rotor-flux-based deadbeat direct torque control of induction machines," *IEEE Trans. Ind. Appl.*, vol. 39, no. 4, pp. 1093–1101, Jul. 2003.

[19] Y. Nie, I. P. Brown, and D. C. Ludois, "Deadbeat-direct torque and flux control for wound field synchronous machines," *IEEE Trans. Ind. Electron.*, vol. 65, no. 3, pp. 2069–2079, Mar. 2018.

[20] M. Hinkkanen, H. A. A. Awan, Z. Qu, T. Tuovinen, and F. Briz, "Current control for synchronous motor drives: Direct discrete-time pole-placement design," *IEEE Trans. Ind. Appl.*, vol. 52, no. 2, pp. 1530–1541, Mar./Apr. 2016.

[21] A. Guagnano, G. Rizzello, F. Cupertino, and D. Naso, "Robust control of high-speed synchronous reluctance machines," *IEEE Trans. Ind. Appl.*, vol. 52, no. 5, pp. 3990–4000, Sep./Oct. 2016.

[22] J. R. Stack, T. G. Habetler, and R. G. Harley, "Fault-signature modeling and detection of inner-race bearing faults," *IEEE Trans. Ind. Appl.*, vol. 42, no. 1, pp. 61–68, Jan. 2006.

[23] X. Sun, B. Su, L. Chen, Z. Yang, X. Xu, and Z. Shi, "Precise control of a four degree-of-freedom permanent magnet biased active magnetic bearing system in a magnetically suspended direct-driven spindle using neural network inverse scheme," *Mech. Syst. Signal Process.*, vol. 88, pp. 36–48, May 2017.

[24] J. Fang, S. Zheng, and B. Han, "AMB vibration control for structural resonance of double-gimbal control moment gyro with high-speed magnetically suspended rotor," *IEEE/ASME Trans. Mechatronics*, vol. 18, no. 1, pp. 32–43, Feb. 2013.

[25] X. Sun, L. Chen, Z. Yang, and H. Zhu, "Speed-sensorless vector control of a bearingless induction motor with artificial neural network inverse speed observer," *IEEE/ASME Trans. Mechatronics*, vol. 18, no. 4, pp. 1357–1366, Aug. 2013.

[26] T. Nussbaumer, P. Karutz, F. Zurcher, and J. W. Kolar, "Magnetically levitated slice motors—An overview," *IEEE Trans. Ind. Appl.*, vol. 47, no. 2, pp. 754–766, Mar./Apr. 2011.

[27] S.-C. Yang and G.-R. Chen, "High-speed position-sensorless drive of permanent-magnet machine using discrete-time EMF estimation," *IEEE Trans. Ind. Electron.*, vol. 64, no. 6, pp. 4444–4453, Jun. 2017.

**YU-LIANG HSU** (M'17) received the B.S. degree in automatic control engineering from Feng Chia University, Taichung, Taiwan, in 2004, and the M.S. and Ph.D. degrees in electrical engineering from National Cheng Kung University, Tainan, Taiwan, in 2007 and 2011, respectively. He is currently an Associate Professor with the Department of Automatic Control Engineering, Feng Chia University, Taiwan. His research interests include computational intelligence, biomedical engineering, nonlinear system identification, and wearable intelligent technology.

**PO-HUAN CHOU** was born in Taipei, Taiwan, in 1982. He received the B.S. degree from Feng Chia University, Taiwan, in 2005, and the M.S. and Ph.D. degree from National Dong Hwa University, Taiwan, in 2007 and 2011, respectively, all in electrical engineering. He is currently with the Industrial Technology Research Institute. His research interests include servo drive systems, intelligent control, DSP-based control systems, and motion control.
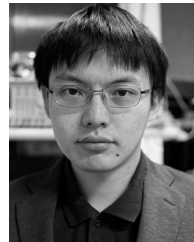
**JYUN-YOU CHEN** was born in Taichung, Taiwan, in 1992. He received the B.S. degree in communication engineering from Feng Chia University, Taiwan, in 2015, and the M.S. degree in mechanical engineering from National Central University, Taiwan, in 2017. He is currently pursuing the Ph.D. degree and dissertator in mechanical engineering with National Taiwan University, Taiwan. His research interests include motor drive and control systems.

**SHIH-CHIN YANG** (S'10–M'12–SM'18) was born in Taiwan. He received the M.S. degree in mechanical engineering from National Taiwan University, Taiwan, in 2007, and the Ph.D. degree from the University of Wisconsin-Madison, Madison, WI, USA, in 2011. From 2011 to 2015, he was a Research Engineer with the Texas Instruments Motor Laboratory, Dallas, TX, USA. He is currently an Assistant Professor with National Taiwan University, Taiwan, with the responsibility on the development of motor drive and motor control technology. His research interests include motor drive, power electronics, and control systems. Dr. Yang was the recipient of the IEEE Industry Applications Society Industrial Drive Committee First Prize Paper Award, in 2011.

**GUAN-REN CHEN** (S'17) was born in Taiwan. He received the M.S. degree in opto-mechatronics engineering from National Central University, Taoyuan, Taiwan, in 2014. He is currently pursuing the Ph.D. degree in mechanical engineering with National Taiwan University, Taipei, Taiwan. His research interests include control systems, motor drives, and intelligent vehicles.

• • •